



# Single-end-access distributed strain sensing with wide dynamic range using higher-speed Brillouin optical correlation-domain reflectometry

Yosuke Mizuno<sup>1\*</sup>, Neisei Hayashi<sup>2</sup>, Hideyuki Fukuda<sup>3</sup>, and Kentaro Nakamura<sup>1</sup>

<sup>1</sup>*Institute of Innovative Research, Tokyo Institute of Technology, Yokohama 226-8503, Japan*

<sup>2</sup>*Research Center for Advanced Science and Technology, The University of Tokyo, Meguro, Tokyo 153-8904, Japan*

<sup>3</sup>*Servo Laboratory, FANUC Corporation, Oshino, Yamanashi 401-0597, Japan*

\*E-mail: [ymizuno@sonic.pi.titech.ac.jp](mailto:ymizuno@sonic.pi.titech.ac.jp)

Received February 24, 2017; revised April 10, 2017; accepted May 8, 2017; published online June 13, 2017

Single-end-access real-time fiber-optic distributed strain sensing has recently been demonstrated using an ultrahigh-speed configuration of Brillouin optical correlation-domain reflectometry (BOCDR). Its extremely high sampling rate was, however, achieved at the cost of a limited strain dynamic range (<0.2%). Here, by employing a noise-floor compensation technique, we develop a new cost-effective higher-speed configuration of BOCDR with a wide strain dynamic range (up to 2.0%; evaluated by static strain measurement). This value is larger than that of any other BOCDR configuration. Using this configuration, we demonstrate some fundamental distributed strain measurements and breakage detection.

© 2017 The Japan Society of Applied Physics

## 1. Introduction

Brillouin scattering<sup>1)</sup> has been extensively exploited to develop fiber-optic sensors due to the feasibility of distributed strain and temperature measurement. Various kinds of distributed Brillouin sensing techniques have been implemented thus far, including Brillouin optical time-domain analysis (BOTDA),<sup>2–12)</sup> Brillouin optical frequency-domain analysis (BOFDA),<sup>13–16)</sup> Brillouin optical correlation-domain analysis (BOCDA),<sup>17–24)</sup> Brillouin optical time-domain reflectometry (BOTDR),<sup>25–29)</sup> and Brillouin optical correlation-domain reflectometry (BOCDR).<sup>30–36)</sup> Among these techniques, “analysis” systems require injection of two light beams into both ends of a fiber under test (FUT) to induce stimulated Brillouin scattering leading to a high signal-to-noise ratio (SNR). In contrast, “reflectometry” systems, which operate based on spontaneous Brillouin scattering, require injection of a light beam into only one end of an FUT. In general, two-end-access analysis systems pose two major problems. First, they are lacking in convenience for practically embedding the sensors into materials and structures; furthermore, the measurement can no longer be performed when extremely high loss or breakage occurs at a point along the FUT. Although some quasi-one-end-access configurations<sup>16,21,22)</sup> have been developed by using the Fresnel reflection at the open end of an FUT, the measurement difficulties associated with a breakage point cannot be perfectly overcome. The second problem is that a relatively expensive electro-optic modulator (EOM), such as a single-sideband modulator, is often needed to accurately produce the frequency difference between the two light beams (pump and probe).<sup>3–18,20–24)</sup> Moreover, most configurations require an additional EOM for optical pulse generation<sup>2–12)</sup> (also true for BOTDR)<sup>25–29)</sup> or chopping for lock-in detection.<sup>17,18,20–24)</sup> Although a time-division pump–probe generation scheme<sup>19)</sup> does not require an EOM for pump/probe generation, the driving current of the laser diode (LD) needs to be precisely controlled. Thus, considering the practical convenience and cost efficiency, here we focus on BOCDR.

BOCDR is known to be an inherently single-end-access sensing technique with high spatial resolution, system simplicity, and cost efficiency, but conventionally, its sampling

rate was limited to 19 Hz due to the relatively slow frequency sweeping.<sup>32)</sup> In 2016, we developed an ultrahigh-speed configuration of BOCDR,<sup>38)</sup> in which the Brillouin gain spectrum (BGS) in the time domain was approximated by a one-period sinusoidal waveform. The Brillouin frequency shift (BFS) was converted into its phase delay, which was subsequently converted into a voltage so that the BFS information can be directly obtained. In this configuration, a strain sampling rate of up to 100 kHz at an arbitrary position was experimentally verified. However, the strain dynamic range was limited to 0–0.2% because of the nature of phase detection. Another high-speed configuration of BOCDR exploits the spectral power of the BGS,<sup>39,40)</sup> but its strain dynamic range was narrower than 0–0.1% because of the limited linear range of the BGS slope. Note that even the widest strain dynamic range of lower-speed BOCDR configurations was 0–0.7%,<sup>35,36)</sup> limited by the non-negligible correlation-peak sidelobes (the influence of which can be mitigated by apodization).<sup>35)</sup>

In this work, we develop a new cost-effective higher-speed configuration of BOCDR with a wide strain dynamic range of up to 2.0%. Here, the frequency sweeping for acquiring the BGS is performed at higher speed without using the inherent sweeping function of an electrical spectrum analyser (ESA), which is used only to detect the signal power at a fixed frequency component. The noise caused by the external frequency sweeping is suppressed by obtaining the differential signal between periods of operation with and without the Brillouin signal, resulting in a high SNR and enhanced strain dynamic range. The additionally required main devices only include a relatively low-performance frequency sweeper [or a standard voltage-controlled oscillator (VCO)] and an inexpensive sound board connected to a computer, thereby maintaining the system simplicity and cost efficiency. Note that this work is an evolutionary version of our previous work published in a conference proceeding,<sup>41)</sup> where similar experimental results are presented but not in detail because of the strictly limited space. Here, mainly focusing on the strain dynamic range, more detailed background, experimental conditions, and discussions are described; furthermore, some experimental results on breakage detection using this configuration are presented for the first time.

## 2. Principles and methods

BOCDR operates based on the controlled correlation of continuous light beams. As described in detail in literatures,<sup>30,31)</sup> by sinusoidally modulating the frequencies of pump light and reference light at modulation frequency ( $f_m$ ), so-called correlation peaks<sup>37)</sup> (which can be regarded as sensing points) are periodically generated in the FUT. The measurement range  $d_m$  corresponds to the interval between the correlation peaks, which is in inverse proportion to  $f_m$ , as follows:<sup>31)</sup>

$$d_m = \frac{c}{2nf_m}, \quad (1)$$

where  $c$  is the velocity of light in a vacuum and  $n$  is the refractive index of the fiber core. By sweeping  $f_m$ , the correlation peak can be scanned along the FUT to derive a BGS or BFS distribution. The spatial resolution  $\Delta z$  is expressed as<sup>31)</sup>

$$\Delta z = \frac{c\Delta v_B}{2\pi n f_m \Delta f}, \quad (2)$$

where  $\Delta v_B$  is the Brillouin bandwidth [ $\sim 30$  MHz in silica single-mode fibers (SMFs)] and  $\Delta f$  is the modulation amplitude of the optical frequency. The upper limit of  $\Delta f$  is half the BFS of the FUT due to the Rayleigh noise.<sup>30,31)</sup> By the sweeping speed of an ESA, the sampling rate including data acquisition to the computer was limited to 19 Hz.<sup>32)</sup> In the meantime, the maximal measurable strain experimentally confirmed was approximately 0.1% in a slope-assisted configuration,<sup>39)</sup> 0.2% in an ultrahigh-speed configuration,<sup>38)</sup> 0.3% in a temporal gating scheme,<sup>33)</sup> and 0.7% in an intensity-modulation-based apodization scheme<sup>35)</sup> or in a lock-in detection scheme.<sup>36)</sup>

The experimental setup of the newly configured BOCDR is schematically shown in Fig. 1. The fiber-optic parts were almost the same as those in a conventional setup.<sup>34)</sup> After optical-to-electrical conversion of the heterodyned Brillouin signal using a photo detector (PD), the BGS was acquired at high speed by converting the signal from the frequency domain to the time domain (note that this step is essentially the same as that in Ref. 38). The Brillouin signal was mixed with the output of a microwave frequency sweeper (MFS); its maximal repetition rate was 50 Hz in this experiment, which can be enhanced further by employing a higher-performance MFS or a VCO. The frequency of the MFS was repeatedly swept for several hundred megahertz to scan the BGS in the frequency domain. The power at a fixed frequency component (carefully selected so that the whole BGS might be covered even when strain or temperature change was applied) of the mixed signal was subsequently output from the ESA using a zero-span mode, and the BGS was repeatedly reproduced in the time domain. Needless to say, the BGS acquisition must be slower than the calculation time required for the BFS derivation from the BGS (in our previous setup,<sup>38)</sup> the BGS was then converted into a one-period sinusoidal waveform to achieve an even higher sampling rate at the cost of the limited strain dynamic range, but here we did not perform this step to maintain a wider dynamic range). Next, the BGS signal in the time domain is input to the computer via an inexpensive sound board (ASUSTek XONAR U7) and monitored using a virtual oscilloscope triggered at the repetition frequency of the MFS. The BGS was observed

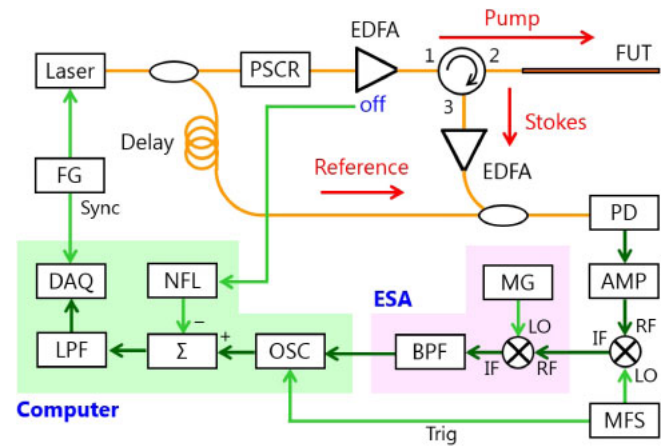


**Fig. 1.** (Color online) Experimental setup of high-speed BOCDR. AMP, amplifier; BPF, band-pass filter; DAQ, data acquisition; EDFA, erbium-doped fiber amplifier; ESA, electrical spectrum analyzer; FG, function generator; FUT, fiber under test; IF, intermediate frequency; LO, local oscillator; LPF, low-pass filter; MFS, microwave frequency sweeper; MG, microwave generator; NFL, noise floor; OSC, oscilloscope; PD, photo detector; PSCR, polarization scrambler; RF, radio frequency.

on a real-time basis, but was largely distorted because of the considerable intensity noise of the MFS output, which was dependent on the output voltage (or frequency). To suppress this noise and clearly observe the BGS, the differential signal between periods of operation with and without the Brillouin signal (i.e., between the two spectra for which the 980 nm pump LD of the EDFA in the Brillouin-pump path is and is not working) was calculated; after low-pass filtering, it was finally acquired as the BGS used for the measurements (note that this noise-floor compensation technique was not required in the ultrahigh-speed configuration,<sup>38)</sup> in which the distorted BGS was directly approximated by a sinusoidal waveform; this was feasible because the frequency span was significantly limited).

## 3. Experimental results

### 3.1 Fundamental characterization

First, we verified that the local BGS can be correctly observed at 50 Hz (maximal repetition rate of the MFS). A 7.0 m long silica SMF (composed of a 0.8 m long pigtail of an optical circulator connected to a 6.2 m long SMF using an FC/APC adaptor) was used as the FUT. The open end was cut at an angle of  $8^\circ$  in order to suppress the Fresnel reflection. The modulation frequency  $f_m$  was set to 13.536 MHz, with a correlation peak located at the point 4.7 m away from the circulator. The measurement range  $d_m$  was calculated to be 7.6 m according to Eq. (1). The modulation amplitude  $\Delta f$  was set to 0.5 GHz, resulting in a theoretical spatial resolution  $\Delta z$  of  $\sim 0.15$  m from Eq. (2). The ratio of the measurement range to the spatial resolution was 51, which can be extended to  $\sim 570$  simply by increasing  $\Delta f$  to half of the BFS, i.e.,  $\sim 5.4$  GHz (the  $\Delta f$  values were kept below 1.5 GHz in this paper to avoid damage to the LD, which was not designed for such modulation use). The 64th-order correlation peak was used, and the temperature of the room was 18 °C.

The green curve in Fig. 2(a) shows the direct output from the ESA, which suffers from so much noise that the BFS cannot even be determined. Note that the vertical axis was normalized in a linear scale so that the maximal voltage of

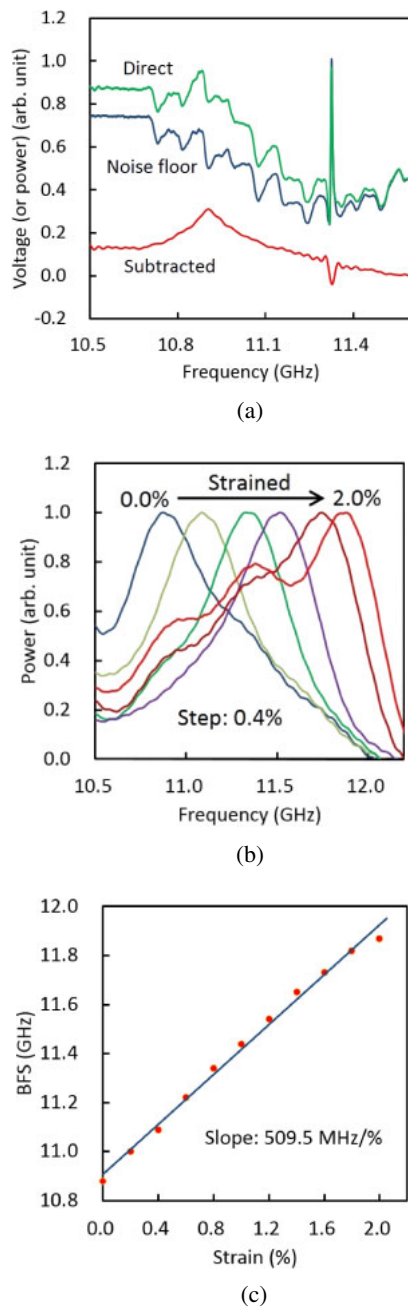


**Fig. 2.** (Color online) (a) Normalized direct output from the ESA (green), noise floor (blue), and the intrinsic BGS obtained as their difference (red). (b, c) Measured BGS and BFS dependences on a relatively large strain of up to 2.0%, respectively. In (c), the orange solid circles are measured points, whereas the blue line is a linear fit.

this spectrum became 1. To suppress this noise, the noise floor, i.e., the spectrum when the EDFA in the pump path was switched off, was recorded [blue curve in Fig. 2(a)] and subtracted from the ESA output, resulting in the intrinsic BGS as shown as the red curve in Fig. 2(a). The dip at  $\sim 11.3$  GHz, which originates from the sharp spectral noise due to the frequency range switching of the MFS, can be flattened with an appropriate low-pass filter (LPF). Thus, it was confirmed that the local BGS was obtained at 50 Hz (we confirmed that a  $>200$ -Hz sampling rate can be achieved simply by replacing the MFS with a VCO; refer to Sect. 2 for the limiting factor).

Next, a wide strain dynamic range was demonstrated. The experimental conditions were the same as those for

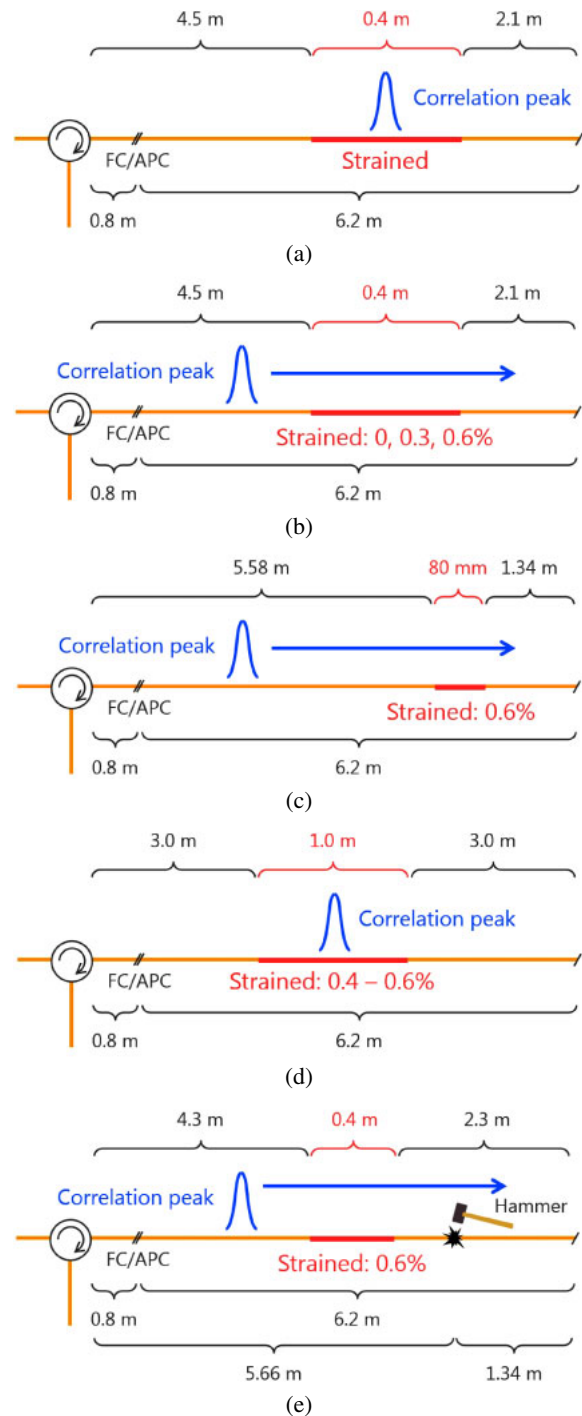


**Fig. 3.** (Color online) Structures of FUTs. (a) Fixed-point measurement of static strain. (b) Distributed measurement with a higher signal-to-noise ratio. (c) Distributed measurement with a higher spatial resolution. (d) Fixed-point measurement of dynamic strain (not sinusoidally applied). (e) Distributed measurement for breakage detection.

evaluating the noise floor described above. In the 7.0 m long SMF used as the FUT, strains of up to 2.0% were applied to a 0.4 m long section (4.5–4.9 m away from the circulator) fixed on a translation stage [Fig. 3(a)]. The correlation peak was located at the midpoint of the strained section. The average of 5 measurements revealed the sampling rate of 10 Hz. Figure 2(b) shows the measured BGS dependence on strain. Note that all the BGSs were normalized. With increasing strain, the BGS shifted to a higher frequency. At 2.0% strain, the translation stages began to slightly slip, at which point the

correct amount of strain was not applied; besides, at such large strain, considerable optical loss was engendered at the fixed (and pressed) positions, resulting in a weak BGS, which was distorted if normalized. Figure 2(c) shows the BFS dependence on strain, which was almost linear. The slope calculated using the data (excluding that of the 2.0% strain) was 509.5 MHz/%, which moderately agrees with the previously reported values at 1550 nm.<sup>30)</sup> In this manner, the wide strain dynamic range of ~2.0% was demonstrated. The maximal measurable strain, which is about three times the largest value previously reported for BOCDR,<sup>35,36)</sup> is even close to the fracture strain of silica SMFs, which is generally several percent.

**3.2 Distributed and dynamic strain measurements**

Distributed measurements were subsequently demonstrated. First, a 7.0 m long silica SMF was used as the FUT, in which strains of 0.3 and 0.6% were applied to a 0.4 m long section (4.5–4.9 m) [Fig. 3(b)]. The modulation frequency  $f_m$  was swept from 13.406 to 13.601 MHz. The measurement range  $d_m$  was calculated to be ~7.6 m. The modulation amplitude  $\Delta f$  was set to 0.5 GHz, corresponding to the nominal spatial resolution  $\Delta z$  of ~0.15 m. The sampling rate for obtaining one BGS was 50 Hz and the number of sensing points was set to 200, leading to a measurement time of ~4 s. The measured BGS distributions (normalized) are shown in Figs. 4(a)–4(c), and the corresponding BFS distributions are shown in Fig. 4(d), where the strained sections were correctly detected with a high SNR. The non-normalized data are discussed in the following Section (i.e., breakage detection).

Next, a 0.6% strain was applied to an 80 mm long section (5.58–5.66 m) of the same FUT [Fig. 3(c)], and  $\Delta f$  was set to 1.5 GHz, corresponding to  $\Delta z$  of ~48 mm. The measured BGS and BFS distributions are shown in Figs. 4(e) and 4(f), respectively, and the magnified view of the latter around the strained section is shown in Fig. 4(g). Although the SNR deteriorated because of the enhanced spatial resolution, the strained section was nevertheless successfully detected. Note that the plot pattern slightly varies measurement by measurement and that the non-sharp BFS change is sometimes obtained probably because of the influence of the strain distribution inside the glue.

We then demonstrated the system’s capacity for dynamic strain sensing. A 0.4% static strain was applied in advance to a 1.0 m long section (3.0–4.0 m) of a 7.0 m long silica SMF [Fig. 3(d)]; the static strain was applied because it was difficult to stably apply dynamic strains to an unstrained section. Dynamic strains at 2.2 and 4.0 Hz were then applied to the strained section, not sinusoidally, using a rotor with a 33 mm long arm (Fig. 5). By setting  $f_m$  to 13.503 GHz, the correlation peak was placed at the midpoint of the strained section ( $d_m \approx 7.6$  m). The spatial resolution  $\Delta z$  was ~0.36 m ( $\Delta f = 0.2$  GHz), and the sampling rate was 50 Hz. No averaging was performed. The measured temporal variations of the BGS and BFS at 2.2 Hz [Figs. 6(a) and 6(b)] and at 4.0 Hz [Figs. 6(c) and 6(d)] indicate that the dynamic strains were successfully detected with a much higher SNR than that of a previous report.<sup>32)</sup>

We here discuss the measurement error of this system by comparing it with that of the ultrahigh-speed configuration of BOCDR.<sup>38)</sup> As already described in the Introduction, in the ultrahigh-speed configuration, the BFS is converted into the

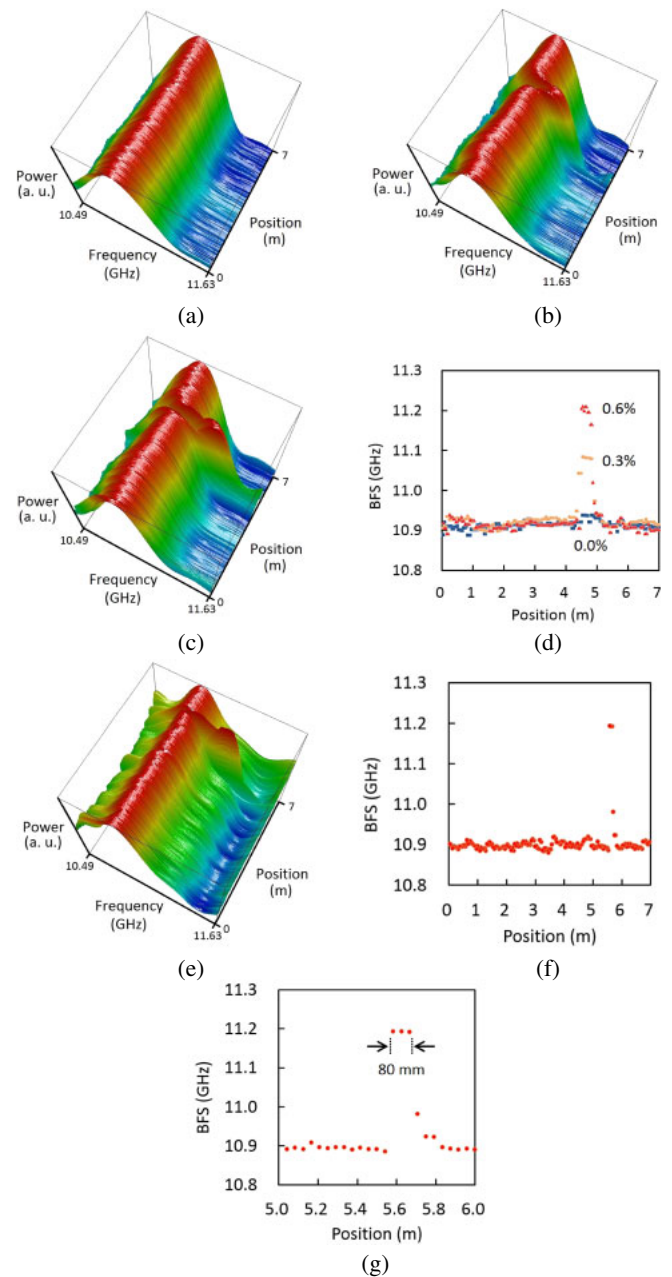


**Fig. 4.** (Color online) Distributed measurement results. (a, b, c) BGS distributions for locally applied strains of 0.0, 0.3, and 0.6%, respectively. (d) Corresponding BFS distributions. (e) BGS distribution for a locally applied 0.6% strain. (f) Corresponding BFS distribution and (g) its magnified view.

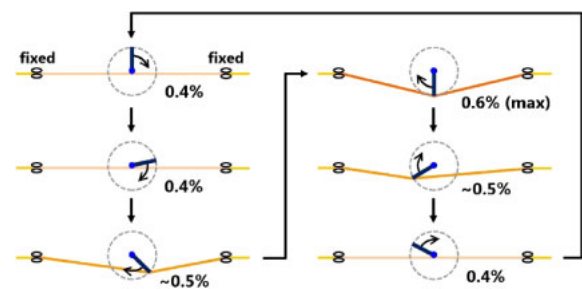


**Fig. 5.** (Color online) Method for applying dynamic strain (0.4–0.6%) to a fixed section of the FUT using an armed rotor.

phase of a sinusoidal waveform. Although we attempt to seek a frequency range which linearly depends on the BFS, the linearity is not perfect, which inevitably results in some

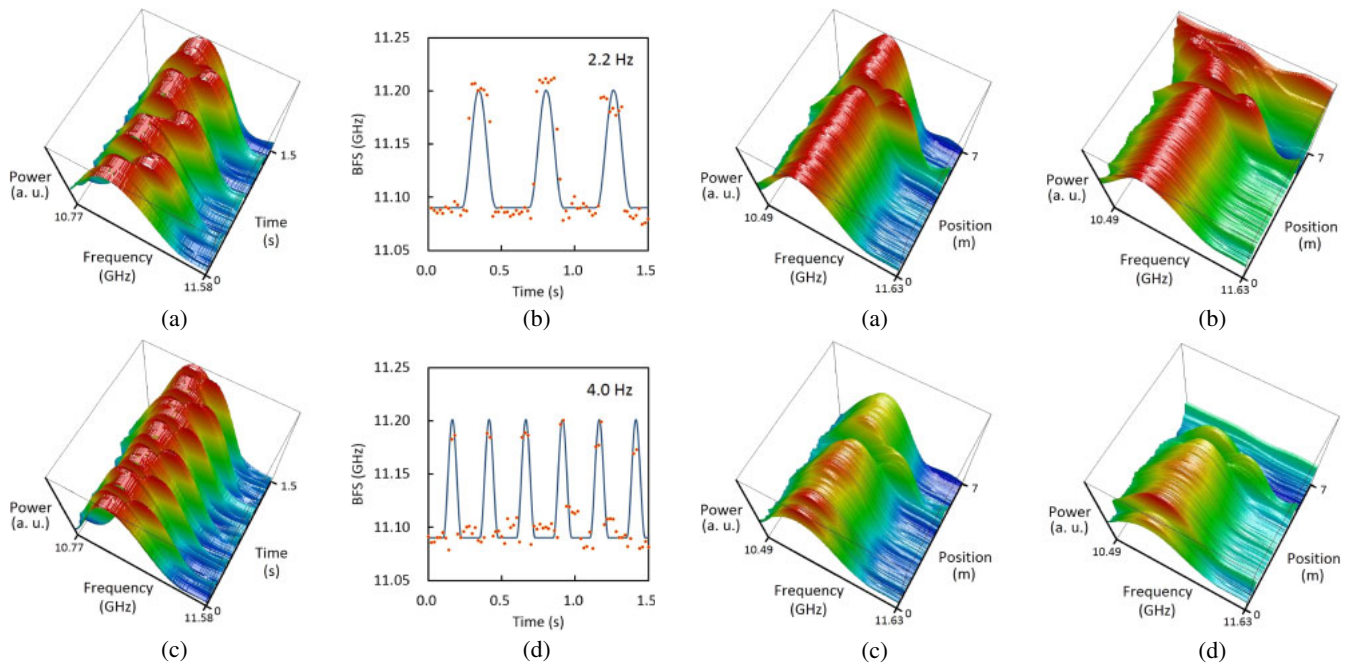


**Fig. 6.** (Color online) Measurement results of dynamic strain. Temporal variation of (a) BGS and (b) BFS at 2.2 Hz, as well as (c) BGS and (d) BFS at 4.0 Hz. The circles are measured points, whereas the solid curves indicate the theoretical trends.

measurement error. On the other hand, in the configuration presented here, the BFS value is directly used for strain evaluation, and consequently, the nonlinearity-induced measurement error can be inherently avoided. The actual sensing error of the system depends on many parameters including the number of averaging. When we need to achieve high-speed measurement, the measurement error becomes relatively serious [see Figs. 6(b) and 6(d)]; however, this error can be suppressed by averaging the data sufficient times.

### 3.3 Breakage detection

We also demonstrated the detection of a breakage point caused during a distributed measurement. This kind of demonstration has not been reported anywhere at least in correlation-domain schemes, and thus it is important to experimentally prove the merit of single-end accessibility (the light reflected at the breakage point may result in deterioration of the measurement). A 7.0 m long silica SMF was used as the FUT, in which a 0.6% strain was applied to a 0.4 m long section (4.3–4.7 m). The measurement range  $d_m$  was  $\sim 7.6$  m ( $f_m$  swept from 13.406 to 13.601 MHz) and the nominal spatial resolution  $\Delta z$  was  $\sim 0.15$  m ( $\Delta f = 0.5$  GHz). Then, during a distributed measurement, the FUT was broken by being crushed with a hammer at a location 5.66 m away from the circulator [Fig. 3(e)]. The normalized BGS distributions along the FUT measured before and after the FUT was broken [Figs. 7(a) and 7(b)] clearly indicate that, when the FUT is broken at a point, the measurement can still continue to the breakage point. However, in the section beyond the breakage point, the normalized spectra were significantly distorted.

Figures 7(c) and 7(d) show the non-normalized data corresponding to Figs. 7(a) and 7(b), respectively. From these figures, the peak-power distributions were derived [Fig. 7(e)]. Before the FUT was broken, a slight spectral jump was observed at 0.8 m, which corresponds to the location at

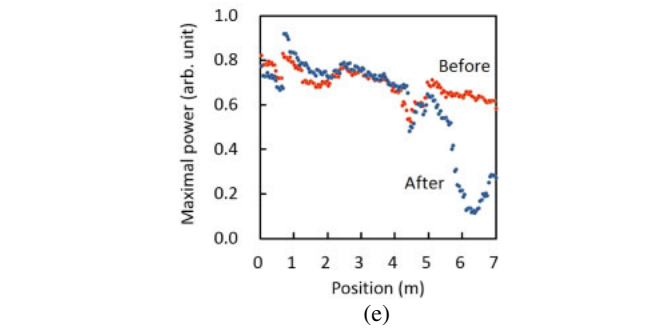


**Fig. 7.** (Color online) Results of breakage detection. (a, b) Normalized and (c, d) non-normalized BGS distributions measured (a, c) before and (b, d) after the FUT was broken at 5.66 m. (e) Peak-power distribution measured before the FUT was broken (red), and after the FUT was broken (blue).

which the FC/APC adaptor connects the pigtail of the circulator and the silica SMF. A spectral dip was also observed at  $\sim 4.5$  m, corresponding to the applied strain. The peak power of the BGS at the strained section becomes lower than that at the unstrained section, because the weak but non-zero Brillouin signals of the correlation peak sidelobes (generally located at the unstrained sections) do not overlap. After the FUT was broken at 5.66 m, and while the spectral jump at 0.8 m and the dip at  $\sim 4.5$  m were maintained, the peak power at the section beyond the breakage point decreased drastically. This is reasonable considering that almost no Brillouin signal returns from where the correlation peak is located, which also explains the distorted normalized spectra [Fig. 7(b)] (this result indicates at the same time that the light reflected at the breakage point does not deteriorate the performance of distributed measurement when we use a hammer, which is closer to a practical situation than a sharp cutter). Therefore, if a certain threshold power is appropriately set [for instance, 0.4 in Fig. 7(e)], we can detect the location of a breakage point on a real-time basis.

### 4. Conclusions

By employing a noise-floor compensation technique, a new higher-speed configuration of BOCDR with a wide strain

dynamic range and cost efficiency was developed and its basic operation was demonstrated. A strain dynamic range of 0–2.0% was experimentally achieved; this value was much wider than that of any other previous configuration. As for the cost efficiency, besides the fact that the experimental setup does not involve EOMs, which are used in most conventional Brillouin sensors, all of the newly employed electrical devices, which include an MFS, filter, mixer, sound board, etc., are relatively inexpensive. Further cost reduction can be achieved by replacing the ESA with a specialized circuit, which also contributes to downsizing the whole system. Brillouin-based breakage detection was also demonstrated for the first time to the best of our knowledge. The sampling rate of this configuration described in this paper was 50 Hz, but we verified that a >200-Hz sampling rate can be achieved simply by replacing the MFS with a VCO, which is over 10 times the highest value of standard configurations. We believe that this cost-effective higher-speed configuration of BOCDR will be of great use for practical distributed strain and temperature sensing with high spatial resolution and wide dynamic range in future.

### Acknowledgments

This work was supported by JSPS KAKENHI Grant Numbers 25709032, 26630180, 25007652, 15J11445, and 17H04930, and by research grants from the Japan Gas Association, the ESPEC Foundation for Global Environment Research and Technology, and the Association for Disaster Prevention Research. The authors are grateful to Heeyoung Lee, Shumpei Shimada, Makoto Shizuka, Kazunari Minakawa, and Hiroki Tanaka (Institute of Innovative Research, Tokyo Institute of Technology) for their experimental assistance.

- 1) G. P. Agrawal, *Nonlinear Fiber Optics* (Academic Press, San Diego, CA, 1995).
- 2) T. Horiguchi and M. Tateda, *J. Lightwave Technol.* **7**, 1170 (1989).
- 3) A. Voskoboinik, J. Wang, B. Shamee, S. R. Nuccio, L. Zhang, M. Chitgarha, A. E. Willner, and M. Tur, *J. Lightwave Technol.* **29**, 1729 (2011).
- 4) R. Bernini, A. Minardo, and L. Zeni, *Opt. Lett.* **34**, 2613 (2009).
- 5) Y. Peled, A. Motil, L. Yaron, and M. Tur, *Opt. Express* **19**, 19845 (2011).
- 6) Y. Peled, A. Motil, and M. Tur, *Opt. Express* **20**, 8584 (2012).
- 7) M. Taki, Y. Muanenda, C. J. Oton, T. Nannipieri, A. Signorini, and F. Di Pasquale, *Opt. Lett.* **38**, 2877 (2013).
- 8) O. Danon, A. Motil, I. Sovran, R. Hadar, and M. Tur, *Proc. SPIE* **9157**, 9157AM (2014).
- 9) M. A. Soto, X. Angulo-Vinuesa, S. Martin-Lopez, S.-H. Chin, J. D. Ania-Castanon, P. Corredera, E. Rochat, M. Gonzalez-Herraez, and L. Thevenaz, *J. Lightwave Technol.* **32**, 152 (2014).
- 10) Y. Dong, L. Chen, and X. Bao, *J. Lightwave Technol.* **30**, 1161 (2012).
- 11) Y. Dong, D. Ba, T. Jiang, D. Zhou, H. Zhang, C. Zhu, Z. Lu, H. Li, L. Chen, and X. Bao, *IEEE Photonics J.* **5**, 2600407 (2013).
- 12) D. Eloorz, Y. Antman, N. Levanon, and A. Zadok, *Opt. Express* **22**, 6453 (2014).
- 13) D. Garus, K. Krebber, F. Schliep, and T. Gogolla, *Opt. Lett.* **21**, 1402 (1996).
- 14) R. Bernini, A. Minardo, and L. Zeni, *IEEE Photonics J.* **4**, 48 (2012).
- 15) A. Minardo, R. Bernini, and L. Zeni, *IEEE Photonics Technol. Lett.* **26**, 387 (2014).
- 16) A. Wosniok, Y. Mizuno, K. Krebber, and K. Nakamura, *Proc. SPIE* **8794**, 879431 (2013).
- 17) K. Hotate and T. Hasegawa, *IEICE Trans. Electron.* **E83-C**, 405 (2000).
- 18) K. Y. Song, Z. He, and K. Hotate, *Opt. Lett.* **31**, 2526 (2006).
- 19) K. Y. Song and K. Hotate, *IEEE Photonics Technol. Lett.* **19**, 1928 (2007).
- 20) W. Zou, Z. He, and K. Hotate, *Opt. Express* **17**, 1248 (2009).
- 21) K.-Y. Song and K. Hotate, *IEEE Photonics Technol. Lett.* **20**, 2150 (2008).
- 22) J. H. Jeong, K. H. Chung, S. B. Lee, K. Y. Song, J. M. Jeong, and K. Lee, *Opt. Express* **22**, 1467 (2014).
- 23) W. Zou, C. Jin, and J. Chen, *Appl. Phys. Express* **5**, 082503 (2012).
- 24) C. Zhang, M. Kishi, and K. Hotate, *Appl. Phys. Express* **8**, 042501 (2015).
- 25) T. Kurashima, T. Horiguchi, H. Izumita, S. Furukawa, and Y. Koyamada, *IEICE Trans. Commun.* **E76-B**, 382 (1993).
- 26) M. N. Alahbabi, Y. T. Cho, and T. P. Newson, *Meas. Sci. Technol.* **15**, 1544 (2004).
- 27) J. Geng, S. Staines, M. Blake, and S. Jiang, *Appl. Opt.* **46**, 5928 (2007).
- 28) A. Masoudi, M. Belal, and T. P. Newson, *Opt. Lett.* **38**, 3312 (2013).
- 29) G. Tu, X. Zhang, Y. Zhang, Z. Ying, and L. Lv, *Electron. Lett.* **50**, 1624 (2014).
- 30) Y. Mizuno, W. Zou, Z. He, and K. Hotate, *Opt. Express* **16**, 12148 (2008).
- 31) Y. Mizuno, W. Zou, Z. He, and K. Hotate, *J. Lightwave Technol.* **28**, 3300 (2010).
- 32) Y. Mizuno, Z. He, and K. Hotate, *IEEE Photonics Technol. Lett.* **21**, 474 (2009).
- 33) Y. Mizuno, Z. He, and K. Hotate, *Opt. Express* **17**, 9040 (2009).
- 34) Y. Mizuno, Z. He, and K. Hotate, *Appl. Phys. Express* **2**, 062403 (2009).
- 35) S. Manotham, M. Kishi, Z. He, and K. Hotate, *Proc. SPIE* **8351**, 835136 (2012).
- 36) Y. Yao, M. Kishi, and K. Hotate, *Appl. Phys. Express* **9**, 072501 (2016).
- 37) K. Hotate and Z. He, *J. Lightwave Technol.* **24**, 2541 (2006).
- 38) Y. Mizuno, N. Hayashi, H. Fukuda, K. Y. Song, and K. Nakamura, *Light: Sci. Appl.* **5**, e16184 (2016).
- 39) H. Lee, N. Hayashi, Y. Mizuno, and K. Nakamura, *IEEE Photonics J.* **8**, 6802807 (2016).
- 40) H. Lee, N. Hayashi, Y. Mizuno, and K. Nakamura, *Opt. Express* **24**, 29190 (2016).
- 41) Y. Mizuno, N. Hayashi, H. Fukuda, and K. Nakamura, *Proc. SPIE* **9634**, 96342V (2015).